ARTICLE

New insights about the origin of the Shilu Fe-Cu-Co deposit, Hainan Island, South China, with emphasis on the regional metallogeny

Wei Terry Chen[1,2] · Mei-Fu Zhou[1] · Yanwen Tang[1]

Abstract

The giant Shilu Fe-Cu-Co deposit in Hainan Island, South China, which was structurally and hydrothermally superimposed, is mainly hosted in highly metasomatized dolostones/marbles of the ~900 Ma Shilu Group. This study confirmed that the ore bodies are originally strata-bound and epigenetic, but do not have spatial relations with any coeval intrusions. In this study, the paragenetic sequence of the pre-deformation mineralization is refined and consists of early Ca-silicate alteration (I), Fe (II), and Cu-Co (III) mineralization stages, followed by multiple overprints and/or undeformed veins (stage IV). Our new oxygen and in situ Pb–S isotopic results for stages I to III show that the mineralizing fluids were initially magmatic-hydrothermal but have undergone variable degrees of interaction with country rocks during mineralization. On the other hand, stage IV fluids have in situ Pb–S isotopic compositions indicative of significant contributions of early-stage components through secondary re-mobilization. These features, in combination with chemical compositions of Fe oxides (e.g., elevated Ti in hematite), strongly argue that the Shilu deposit does not belong to BIF as previously considered, but is typical of magmatic-hydrothermal IOCG deposits. New sulfide Re-Os isotopic data show that the major Fe-Cu-Co mineralization formed at 780 ± 24 Ma (MSWD $= 0.62$). The deposit is confirmed to be broadly comparable to Neoproterozoic IOCG deposits in the Ailao Shan-Red River shear zone in terms of timing and nature of mineralization. Given that the shear zone likely extends to Hainan Island, the Shilu deposit is considered to be part of the same IOCG metallogenic belt and similar mineralization along the shear zone may be more widespread than previously thought.

Keywords Shilu deposit · IOCG deposit · Sin Quyen · Ailao Shan-Red River shear zone · Re-Os dating

Introduction

Many polymetallic deposits, particularly Precambrian ones, have been overprinted or modified by multiple tectonothermal events after their formation (e.g., Kangdian Fe-Cu metallogenic province; Zhou et al. 2014). If the nature of primary mineralization and late overprinting events and their relative roles on the formation of the deposits can be reconstructed, then the possible genetic linkages among deposits in particular regions/belts can be comprehensively

✉ Wei Terry Chen

1 State Key Laboratory of Ore Deposit Geochemistry, Institute of Geochemistry, Chinese Academy of Sciences, Guiyang 550081, China

2 University of Chinese Academy of Sciences, Beijing 100049, China

constrained. Such constraints are thus useful for regional exploration, but are often challenging as these deposits are structurally complex and the primary mineralization textures may be partially masked (Slack 2012).

The giant Shilu Fe-Cu-Co deposit in Hainan Island of South China (Fig. 1b), containing 460 Mt Fe ores with 51.2% Fe, 0.012 Mt Co, and 0.08 Mt Cu, has been regarded as the largest high-grade Fe deposit in Asia (Xu et al. 2009; Xiao et al. 2010). However, other Fe-Cu-Co deposits of this type have not been reported in the island so far, and potential correlations with metallogenic events in adjacent regions are open to discussion. This is partially ascribed to the fact that the ores of this deposit are variably deformed or hydrothermally modified (Xu et al. 2015), and most previous studies were based on bulk rocks/ores or mineral separates that likely involve multiple stages of formation (e.g., Xu et al. 2013, 2014, 2015; Yu et al. 2014). As such, some key issues regarding the nature of pre-deformation Fe and Cu-Co mineralization, genetic affinities of Fe oxides, and

Fig. 1 **a**) Tectonic framework of China; **b**) a simplified geological map of the Yangtze and Cathaysia Blocks in the South China Craton (modified from Zhao et al. 2011 and Zhou et al. 2014), showing that the southwestern part of the craton is displaced by the Cenozoic Ailaoshan-Red River shear zone that is extended to Hainan Island; **c**) a simplified geological map of the Shilu deposit (after Xu et al. 2013); **d**) cross-section A–A′ marked in c)
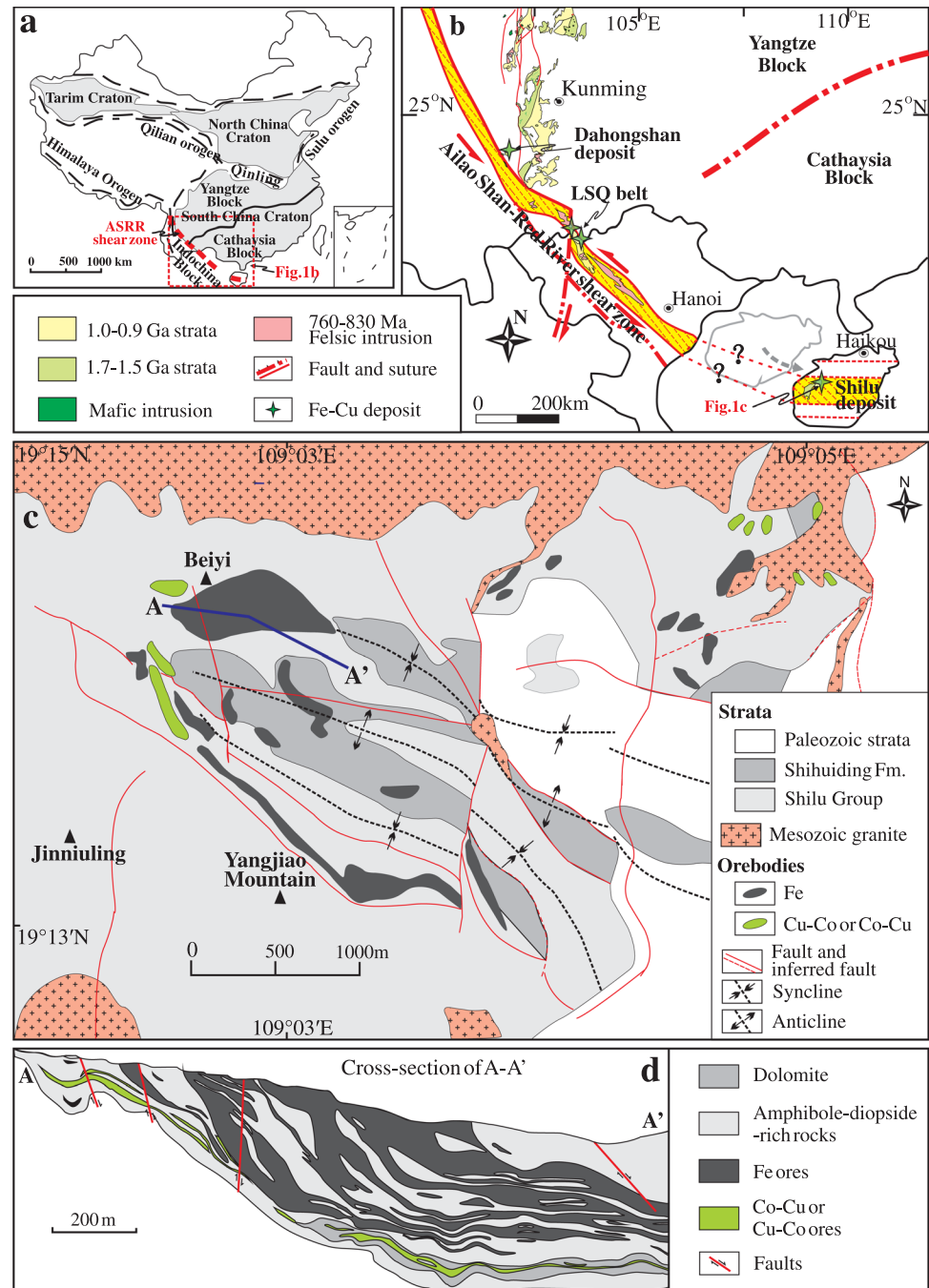
timing of potentially multiple mineralization events have long been matters of debate. Shilu has been considered to be of skarn-type on the basis of the presence of skarn minerals such as garnet and diopside (Zhao et al. 2008), or similar to iron-oxide copper gold (IOCG) deposits due to the metal assemblage (e.g., Fe, Cu, Co, Ni, and Au) (Xu et al. 2008a; Du et al. 2012). In contrast, recent studies concluded that the deposit could represent structurally and hydrothermally reworked banded iron formation (BIF) of Neoproterozoic age (Xu et al. 2013, 2014, 2015; Yu et al. 2014; Wang et al.

2015a), and that the so-called skarn minerals, garnet and diopside, are secondary, likely metamorphic or hydrothermal in origin (e.g., Xu et al. 2013; Yu et al. 2014).

In this contribution, we re-examine the origin of the Shilu deposit with emphasis on textural and in situ geochemical features. Pre-deformation, primary mineralization textures were carefully identified by using optical and scanning electron microscopy (SEM) techniques. Chemical compositions of garnet, diopside, and Fe oxide (hematite/magnetite) from different types of ores were acquired by using electron probe

micro-analyzer (EPMA) and laser ablation-inductively coupled plasma-mass spectrometry (LA-ICP-MS) techniques, in order to reveal the genetic affinity of these minerals (e.g., hydrothermal or BIF Fe oxide; Dupuis and Beaudoin 2011; Dare et al. 2014; Nadoll et al. 2014). In situ U–Pb dating of garnet and Re-Os isochron dating of pyrite from different generations were conducted for the first time to precisely constrain the timing of potentially multiple mineralization/hydrothermal events in the Shilu deposit. Furthermore, in situ sulfide S-Pb isotopic and magnetite/hematite oxygen isotopic compositions, in combination with previously reported fluid inclusion thermometric data, were used to constrain the nature of these mineralization/hydrothermal events. These new results allow us to make a detailed comparison of the Shilu deposit with potentially similar deposits in adjacent regions, thus capable for providing new insights for regional metallogeny.

Geological background

The South China Craton constitutes the Yangtze Block to the northwest and Cathaysia Block to the southeast, amalgamated at ~ 830 Ma along the Jiangnan orogenic belt (Zhao et al. 2011) (Fig. 1a). It is separated from the North China Craton by the Qinling orogenic belt to the north, and the Tibetan Plateau by the Songpan–Gantze terrane to the west (Fig. 1a). The southwestern part of the South China Craton was displaced by the Cenozoic Ailaoshan-Red River (ASRR) shear zone which is a left-lateral continental strike-slip fault (Fig. 1b) and extends for over 1000 km from southeastern Tibet to the Gulf of Tonkin and the South China Sea (Chung et al. 1997; Searle et al. 2010). Recent studies further confirmed that the shear zone likely extends to Hainan Island (Fig. 1b) (Zhou et al. 2014; Zhang et al. 2020). It is notable that voluminous Neoproterozoic (843–751 Ma) felsic intrusions have been identified in the ASRR shear zone (Fig. 1b) (e.g., Hieu et al. 2009; Wang et al. 2016; Li et al. 2018b). These intrusions have geochemical signatures of arc affinity and are commonly suggested to be part of the giant Neoproterozoic magmatic arc belt in the western Yangtze Block which was displaced by the ASRR shear zone (Cai et al. 2015; Li et al. 2018b).

Precambrian geology of Hainan Island

The Precambrian geology of Hainan Island was described in detail in literature (e.g., Xu et al. 2013; Zou et al. 2017), and thus is briefly summarized here. The island is an epicontinental island separated from mainland South China by the Qiongzhou Strait. Tectonically, it was traditionally proposed to be the southernmost part of the South

China Craton (Guangdong BGMR 1988; Li et al. 2002), or to be affiliated to the Indochina Block (Fig. 1a) (Hsü et al. 1990). Recent studies revealed that the northern and southern parts of the island, likely separated by the E-W-trending Changjiang-Qionghai or Jiusuo-Lingshui faults, have affinities with the South China Craton and Indochina Block, respectively (Li et al. 2000, 2002; Xu et al. 2008b; Zhang et al. 2011), consistent with the thesis that the Cenozoic ASRR shear zone likely extended to Hainan Island (Fig. 1b) (e.g., Zhang et al. 2011; Chen et al. 2013; Zhou et al. 2014; He et al. 2018).

The Proterozoic rocks are mainly exposed in the Changjiang region of the western island, including the 1.8–1.45 Ga Baoban and ~ 900 Ma Shilu groups of which the latter is unconformably overlain by the Shihuiding Formation (Fig. 1c) (Xu et al. 2013; Wang et al. 2015b). The Baoban Group is composed dominantly of gneisses and schists, and was considered to be the oldest basement outcropped in this region (Xu et al. 2020). The Shilu Group is composed of quartz-sericite schists, dolostones/marble, and quartzites with subordinate interlayers of slate, jasperite, phyllite, and felsic volcanic rocks, whereas the Shihuiding Formation comprises mainly quartz sandstones with minor phyllite interlayers. The Shihuiding Formation has long been speculated to be Sinian in ages (e.g., Xu et al. 2013 and references therein), but recent studies showed that this formation contains detrital zircon grains with age patterns undistinguishable from those of the Shilu Group (Wang et al. 2015b), thus likely the uppermost part of the Shilu Group. Intrusive rocks in Hainan Island are mainly late Paleozoic to Mesozoic granites (Wang et al. 1991), accounting for more than 40% of the island, whereas Precambrian ones currently documented are only the ca.1.45 Ga granodiorites and monzogranites intruding the Baoban Group (Li et al. 2008).

## Geology of the Shilu Fe-Cu-Co deposit

Host rocks

The Shilu Fe-Cu-Co deposit is located in Changjiang County, western Hainan Island. The ore bodies are mainly hosted in the Shilu Group and/or the Shihuiding Formation (Fig. 1c and d). The Shilu Group comprises six units that are traditionally named as No. 1 to No. 6 from bottom upward. The No. 1, No. 3, and No. 5 units are composed dominantly of quartz-sericite schists; the No. 2 unit comprises dolostones and pyroxene-amphibole-rich rocks; the No. 4 unit consists of quartz schist and quartzite. The No. 6 unit is dominated by dolostones/marbles and pyroxene-amphibole dolostones with subordinate layers of slate, jasperite, phyllite, and felsic volcanic rocks.

Ore bodies

The Fe-Cu-Co ore bodies are mostly strata-bound and mainly hosted in Ca-silicate-rich dolostones/marble (i.e., the "diopside-amphibole-rich rocks"; Xu et al. 2015) and/ or meta-clastic rocks of the No. 6 unit, with minor ores also in the sandstones of the Shihuiding Formation (Figs. 1c and 2a, c). The Fe, Co, and Cu mineralization is unevenly distributed, and hence the ore bodies were traditionally classified as Fe or Cu-Co variants on the basis of relative concentrations of Fe, Cu, and Co (e.g., Fig. 1c and d) (Xu et al. 2013 and references therein). Current exploration reveals 38 Fe and 61 Cu-Co ore bodies (Xu et al. 2009; Xiao et al. 2010), distributed mostly in the Beiyi mine (Fig. 1c). In the mine, both the Fe and Cu-Co ore bodies have similarly angular contacts with their host rocks that are variably rich in
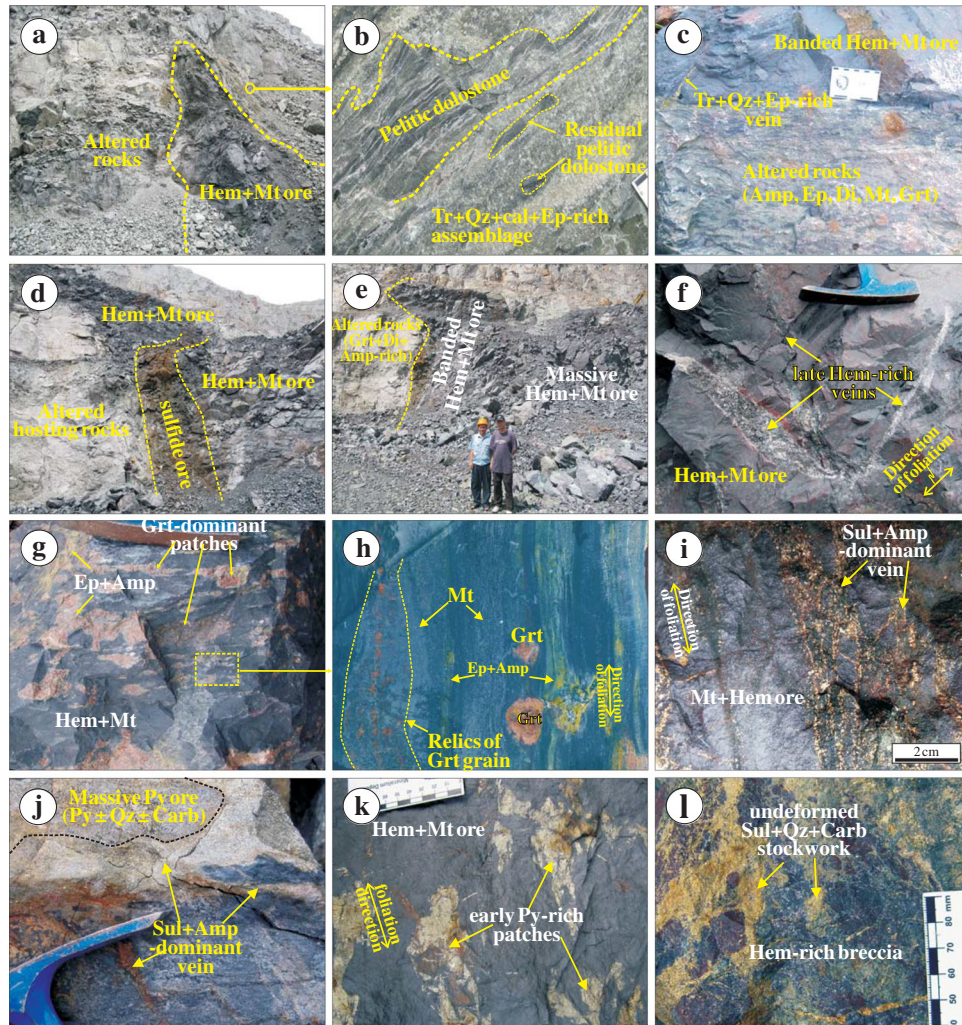
Fig. 2 Disrupted macro-textural relationships of different ores in the Shilu deposit. **a**) Hematite-magnetite ore lens cross-cutting altered host rock; **b**) deformation of early dolostone/marble replaced by an alteration assemblage of amphibole, quartz, and calcite; **c**) transitional contacts between Fe-ores and host rocks. Note that the host rocks are also composed of disseminated magnetite/hematite associated with garnet and diopside that are replaced by amphibole, epidote, calcite, and quartz; **d**) Fe ore body intercepted by Cu-Co-sulfide ore body (or sheet); **e**) angular hematite-magnetite ore body intercepts host rocks. Note that the center is dominated by massive ores, whereas the margin consists mainly of banded ores; **f**) late, undeformed hematite-rich veins crosscutting early Fe ores that are deformed; **g**) banded Fe ores in the margin of a Fe ore body. Note that the mineral patches are elongated due to deformation; **h**) micro-

view of panel (g) showing that although the ores are deformed, the primary texture that early garnet and diopside are replaced by magnetite/hematite, amphibole, and epidote is still preserved; **i**) massive Fe ore crosscut by sulfide-dominant veins. Note that both the Fe ore and sulfide veins are foliated; **j**) both early pyrite-dominant blocks and host rocks were crosscut by late, sulfide-amphibole-dominated veins. Note that both the pyrite block and host rocks are deformed; **k**) xenoliths of early pyrite-rich patches in massive Fe ores. Note that the pyrite-rich patches are replaced by Fe oxides, followed by deformation; **l**) late, undeformed sulfide-rich veins crosscutting early hematite-rich host rocks. Mineral abbreviations: Mt, magnetite; Hem, hematite; Grt, garnet; Ep, epidote; Di, diopside; Qz, quartz; Amp, amphibole; Carb, carbonate; Py, pyrite; Cal, calcite; Ccp, chalcopyrite; Py, pyrite; Tr, tremolite; Po, pyrrhotite; Sul, sulfide

garnet, diopside, and amphibole, and exhibit banded textures (Fig. 2b and c). The Fe and Cu-Co ore bodies are mostly separated, but if together, the former is generally cross-cut by the latter (Fig. 2d). A number of granitoids, porphyries, and mafic dykes of 240–90 Ma (Wang et al. 1991, 2011; Yu et al. 2012) are widely distributed in the mining district and surrounding areas (Fig. 1c). They postdate the Fe-Cu-Co ores, and are responsible for local contact metamorphism forming hornfels (Xu et al. 2009; Yu et al. 2014).

Mineralization styles

Iron ores in the Shilu deposit were generally classified as massive and banded ones based on variable mineral assemblages and ore structures (Fig. 2e), but both types are transitional if associated. The massive Fe ores are distributed mainly in the center of the Fe ore bodies (Fig. 2e and f), and are composed dominantly of hematite, magnetite, and quartz (5 to 30 vol%) with minor barite, sulfides, and/or detritus (total < 5 vol%) (Fig. 3a, b, c, and d). Although the massive ores are variably deformed or metamorphosed, some pre-deformation original textures still survived. For

example, both quartz and detritus (e.g., fragments of sandstone, dolostone, or Fe-rich jasperite) are present as angular or rounded grains cemented by the matrix of hematite and magnetite (Fig. 3a, b, and c). On the other hand, the banded Fe ores occur mostly in the margins of Fe ore bodies where the ores are in angular contact with the diopside-amphibole-rich dolostones that are also variably rich in Fe oxides (Fig. 2e, g, and h). They are generally composed of variable amounts of magnetite/hematite (> 50 vol%), garnet, diopside, amphibole, and calcite with minor epidote, quartz, pyrite, and chalcopyrite (Fig. 3e), and their banded textures are defined by mineral orientation (Fig. 2g and h). Although the banded Fe ores are variably deformed, retained pre-deformation textures clearly show that both the garnet and diopside are corroded or replaced by magnetite/hematite, amphibole, epidote, chlorite, and calcite (Fig. 3e). Both the massive and banded Fe ores have highly variable hematite/magnetite proportions but in most cases hematite dominates (Xu et al. 2015). It is notable that the hematite slightly predates magnetite, as in some Fe ores it is well shown that relatively euhedral hematite grains are surrounded by magnetite matrix (Fig. 3d).
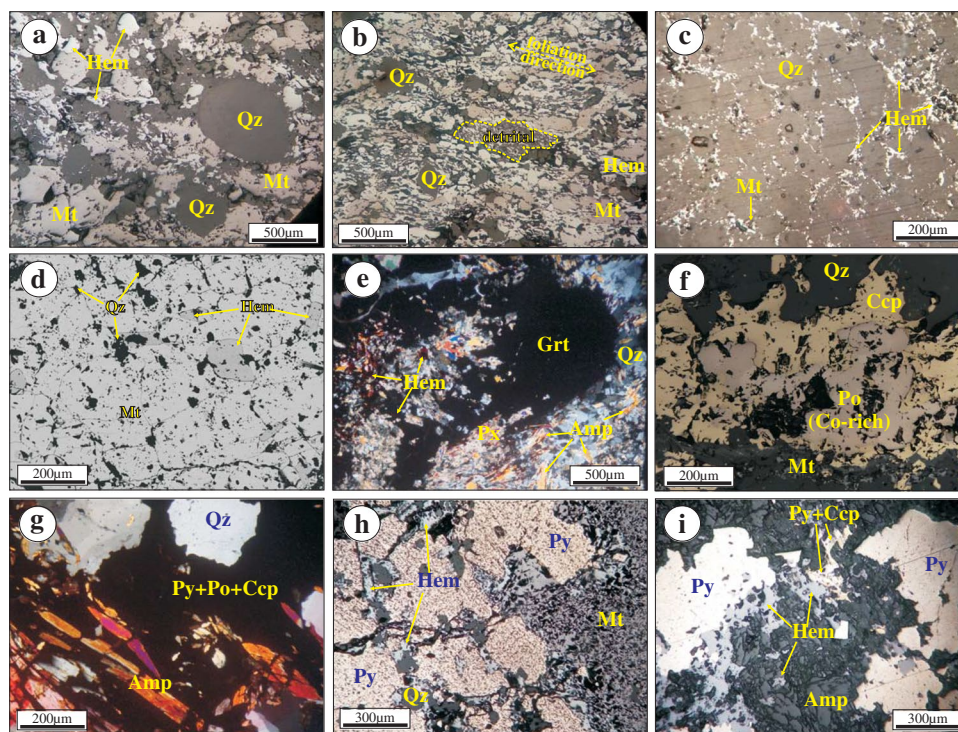
Fig. 3 Micro-textural relationships of different ores in the Shilu deposit. **a**) and **b**) Sub-massive to massive quartz-type Fe ore composed dominantly of subhedral to anhedral magnetite, hematite, and quartz with minor detritus. Note that the quartz grains are corroded, cemented by matrix of hematite and magnetite; **c**) quartz with hematite and minor magnetite on grain boundaries; **d**) magnetite with minor, earlier euhedral hematite and angular quartz; **e**) "Skarn-type" Fe ore where early garnet and diopside grains are replaced by hema-tite, quartz, and amphibole; **f**) sulfide ore with chalcopyrite and Co-rich pyrrhotite replacing early magnetite and quartz; **g**) Cu-Co sulfide ore composed of sulfides and tremolite replacing early quartz; **h**) early sedimentary pyrite patch replaced by hematite and magnetite; **i**) early sedimentary pyrite grains replaced or crosscut by hematite/magnetite, chalcopyrite, pyrite, quartz, and tremolite. The mineral abbreviations are similar to those in Fig. 2

The Cu-Co mineralization was comprehensively investigated by Wang et al. (2015a), and two generations of Cu- or Co-rich sulfides corresponding to two types of Cu-Co ores (i.e., banded and vein-types) were identified. Similarly, this study documented that the major Cu-Co mineralization is also present as disseminations, bands, or vein-stockwork that show clear evidence of overprinting early Fe ores and host rocks (e.g., Fig. 2d, i, and j) but generally predating the foliation (e.g. the early sulfide minerals were elongated). The Co- and Cu-sulfides are dominantly Co-rich pyrite (up to 9 wt% Co; Wang et al. 2015a), Co-rich pyrrhotite, and chalcopyrite (Fig. 3f), associated with variable amounts of amphibole, calcite, dolomite, quartz, chlorite, and micas (Figs. 2i and 3g). The Co-rich pyrite and pyrrhotite are generally sub-euhedral, surrounded by chalcopyrite (Fig. 3f), indicating that chalcopyrite slightly postdates Co-sulfides (Wang et al. 2015a). It is notable that abundant massive pyrite bands or patches are identified in this study and were also reported in Wang et al. (2015a). They are composed mainly of Co-poor pyrite with minor quartz and calcite (e.g., Fig. 2j), and clearly predate the Fe and Co–Cu mineralization. For example, they are locally overprinted or replaced by Fe oxide and Cu-Co-rich sulfides (Figs. 2j, k and 3h, i), indicative of early sedimentary origin as previously proposed (Xu et al. 2013; Yu et al. 2014; Wang et al. 2015a).

Both the Fe and Cu-Co ores in the Shilu deposit, as well as the host rocks, are variably deformed or foliated, as characterized by orientation of minerals (Fig. 2g) or elongation

of mineral patches or veins (Figs. 2h, i, k and 3b). The deformed ores are locally crosscut by abundant sulfide-rich or hematite-rich veins that are not deformed or foliated (Fig. 2f and l).

Paragenetic sequence

The macro- and micro-textural relationships show that although the Fe-Cu-Co ores are variably deformed, some key original textures or mineral paragenesis are still retained (Fig. 2g and h). Our results reveal that early garnet and diopside in the banded Fe ores and nearby pyroxene-amphibole-rich host rocks are disturbed by magnetite/hematite, amphibole, and epidote, followed by elongation related to late deformation or foliation (Fig. 2g and h). Even in the foliated massive Fe ores with minor quartz, the original texture with quartz replaced by Fe oxides is still well retained (Fig. 2a, b, and c). Therefore, on the basis of these identified pre-deformation, micro- and macro-textural relationships, we re-establish a three-stage, paragenetic sequence (Fig. 4) that is different from those previously proposed (e.g., BIF-related; Xu et al. 2014). Stage I is characterized by pre-ore Ca-silicate alteration forming mainly garnet and diopside with minor amphibole, constituting the so-called diopside-amphibole-rich rocks (Xu et al. 2013, 2015). Stage II is the Fe mineralization characterized by formation of abundant hematite and magnetite associated with variable amounts of amphibole, epidote, and calcite. Stage III, the

Fig. 4 Simplified paragenetic sequence of mineralization and alteration in the Shilu deposit
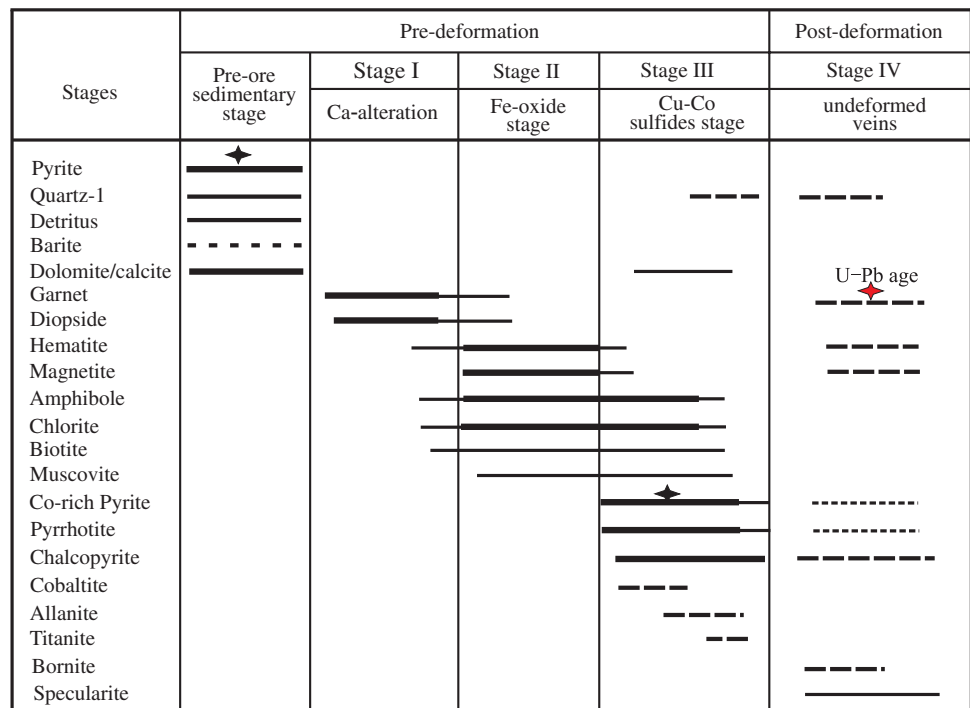
Co–Cu mineralization stage, is characterized by formation of Co-rich pyrite, Co-rich pyrrhotite, and chalcopyrite associated with variable amounts of amphibole, calcite, dolomite, chlorite, and quartz. It is clear that the mineral assemblage of this stage locally overprinted the early Fe ores, followed by late overprints of pervasive deformation and foliation (Figs. 2g, h, I and 3b). The deformed mineral assemblages of stages I, II, and III are crosscut by undeformed veins and/or veinlets (stage IV) that are locally extensively developed (Fig. 2i). These veins are mostly rootless (e.g., Fig. 2f), and consist of diverse mineral assemblages containing variable amounts of hematite/specularite, chalcopyrite, pyrite, pyrrhotite, quartz, amphibole, epidote, garnet, and calcite. The variable assemblages tend to be spatially correlated with those of early components the veins crosscut. For example, the undeformed veins crosscutting Fe ores are commonly dominated by Fe oxides (specularite) (Fig. 2f).

Mineral chemistry

Chemical compositions of diopside and garnet in stage I are obtained by EPMA, whereas trace elemental compositions of magnetite and hematite are measured by LA-ICP-MS. The analytical methods of both EPMA and LA-ICP-MS and the chemical data are all provided in Electronic Supplementary Materials (i.e., Appendix I, ESM Tables 1 and 2, respectively).

Compositions of diopside and garnet

The results show that the garnet grains are essentially solid solutions of grossular (Gr)-andradite (Ad)-pyralspite (Py), ranging in composition from $Ad_{61.6}Gr_{34.7}$ to almost pure andradite ($Ad_{99.8}$), with pyralspite contents mostly less than 4% (ESM Table 1). In most cases, the garnet grains do not exhibit clear zonation under back-scattered electron (BSE) imaging or an optical microscope, but for those with zonations, their rims generally have slightly higher grossular but lower andradite contents than the cores. On the other hand, the diopside grains have compositions with dominant Di components (Di values mostly > 90%), and have an average composition of $Di_{94.6}Hd_{4.5}Jo_{0.8}$ on the basis of 29 analyses.

Trace elemental compositions of Fe oxides

Both magnetite and hematite from the massive and banded Fe ores have been analyzed (ESM Table 2; Fig. 5). Magnetite grains in both types of ores have wide and comparable ranges of Al (~ 10–870 ppm), Ti (~ 1–200 ppm), V (~ 1–70 ppm), Mg (~ 1–1200 ppm), Mn (~ 50–1900 ppm), Co (~ 0.01–20 ppm), and Sn (~ 0.01–7 ppm) with slightly different median values (ESM Table 2; Figs. 5 and 6). The magnetite grains in the banded ones have median values of Al (249 ppm), Sn (0.3 ppm), and Ti (34.1 ppm) higher but Co (2.76 ppm), Ni (3 ppm), and Cr (17 ppm) lower than

Fig. 5 Bimodal diagrams of Al vs. Ti **a**), V vs. Ti **b**), Cr vs. Ti **c**), and Mn vs. Mg **d**). The trace elemental data of IOCG deposits in Kangdian and Longbohe-Sin Quyen (LSQ) belts are cited from Chen et al. (2015) and our unpublished data, respectively
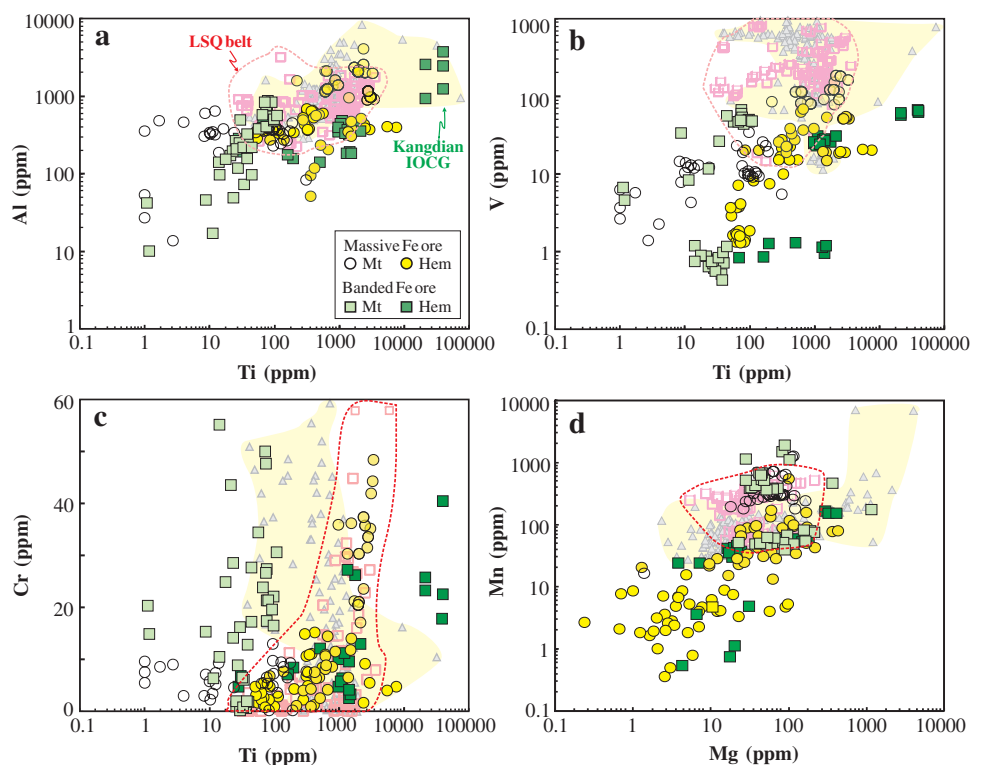
Fig. 6 Box-and-whisker plots of trace elemental compositions of magnetite and hematite (in ppm) from different Fe ores in the Shilu deposit
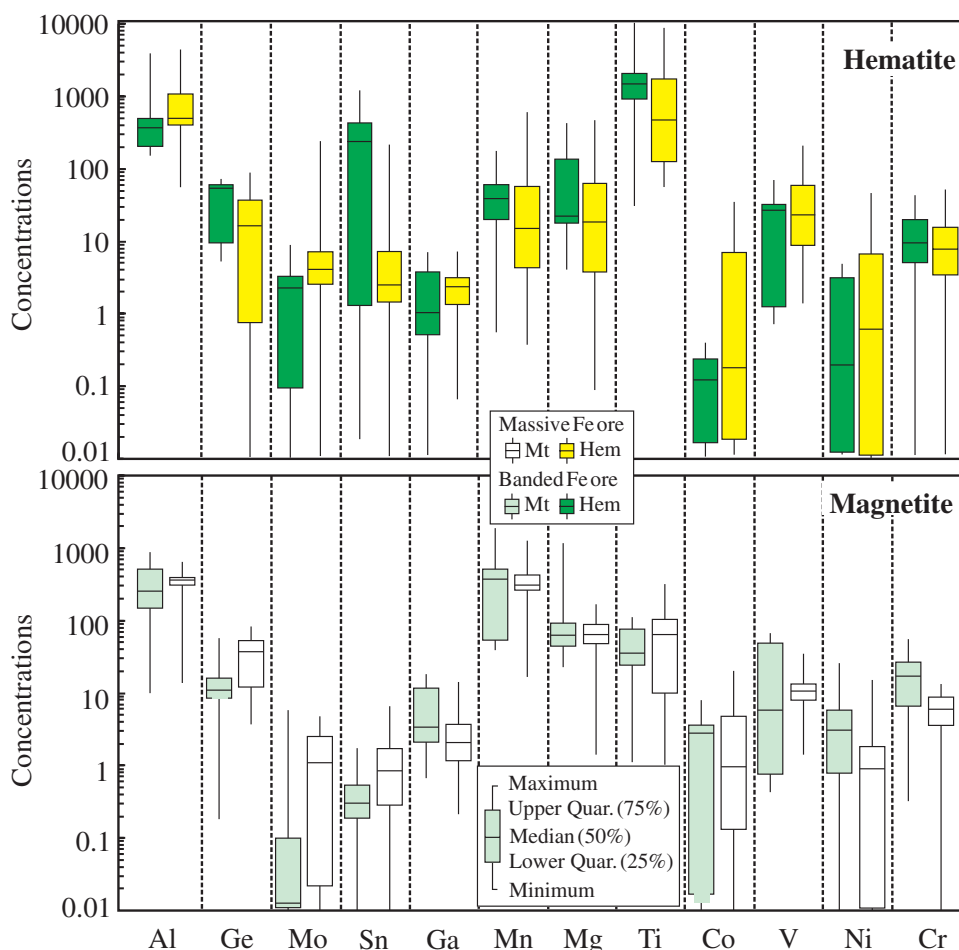
those in massive ones (Fig. 6; ESM Table 2). There are positive correlations of Ti with Al and V (Fig. 5a and b).

The hematite grains from the massive Fe ores have ~50–4000 ppm Al, 0.05–7 ppm Ga, 0.1–430 ppm Mg, 30–7600 ppm Ti, and 0.01–50 ppm Cr, broadly overlapping with those from the banded Fe ores (ESM Table 2; Figs. 5 and 6). However, these grains in the massive Fe ores tend to have slightly higher median values of Co (0.16 ppm) and Ni (0.53 ppm) but lower Ge (15.1 ppm), Sn (2.3 ppm), Mn (13.1 ppm), Ti (421 ppm), and Ga (2.11 ppm) (Fig. 6). In total, hematite in both types of ores has remarkably higher Al, Ti, Mo, and Sn but lower Mn than magnetite (Fig. 5). However, all these analyses of hematite and magnetite show clearly positive correlations of Al, V, and Cr with Ti and Mn with Mg (Fig. 5a, b, c, and d).

Sulfide Re-Os and garnet U–Pb isotopic dating

The detailed analytical procedures for Re-Os and U–Pb dating are available in Appendix I, and the results are provided in Electronic Supplementary Materials (i.e., ESM Tables 3 and 4, respectively).

Sulfide Re-Os isotopic ages

The samples for Re-Os dating include pyrite separates from the early massive pyrite bands and stage III banded-disseminated Cu-Co ores. Both types of pyrite clearly predate the deformation or late undeformed veins, and thus have potential risks of secondary overgrowths (e.g., Fig. 7a). Therefore, only the samples without clear sights of late veins overprints were selected (e.g., Fig. 7b).

Six pyrite separates of the early massive pyrite bands have 0.16 to 41.9 ppb ^{187}Re and 0.02 to 1.28 ppb ^{187}Os. They have ^{187}Re/^{188}Os ratios ranging from 51.2 to 761, much lower than those of typical low-level highly radiogenic sulfides that generally have ^{187}Re/^{188}Os ratios remarkably higher than 5000 (Stein et al. 2001). The relatively low ^{187}Re/^{188}Os ratios indicate that the Re-Os model ages calculated directly from ^{187}Re and ^{187}Os concentrations cannot represent the real ages of these samples. Indeed, such an interpretation is consistent with the highly variable model ages (931–1603 Ma; ESM Table 3), due to high budgets of common Os. Therefore, the age calculation is performed by using conventional isochron methods on the basis of the plots of ^{187}Re/^{188}Os against ^{187}Os/^{188}Os. There is a clear correlation in the plots

Fig. 7 High-resolution back-scattered electronic images of pyrite and garnet from the Shilu deposit. **a**) Euhedral pyrite grain showing core-rim texture. Note that the core (Py I) represents early sedimentary pyrite, over-grown by Co-rich pyrite (Py II) that is closely associated with chalcopyrite; **b**) homogeneous Co-rich pyrite (Py II) associated with chalcopyrite; **c**) and **d**) garnet in Fe-oxide ore, showing complex internal texture indicative of extensive secondary modification. Note that the garnet grains contain abundant mineral inclusions of Fe oxides, amphibole, and/or sulfides
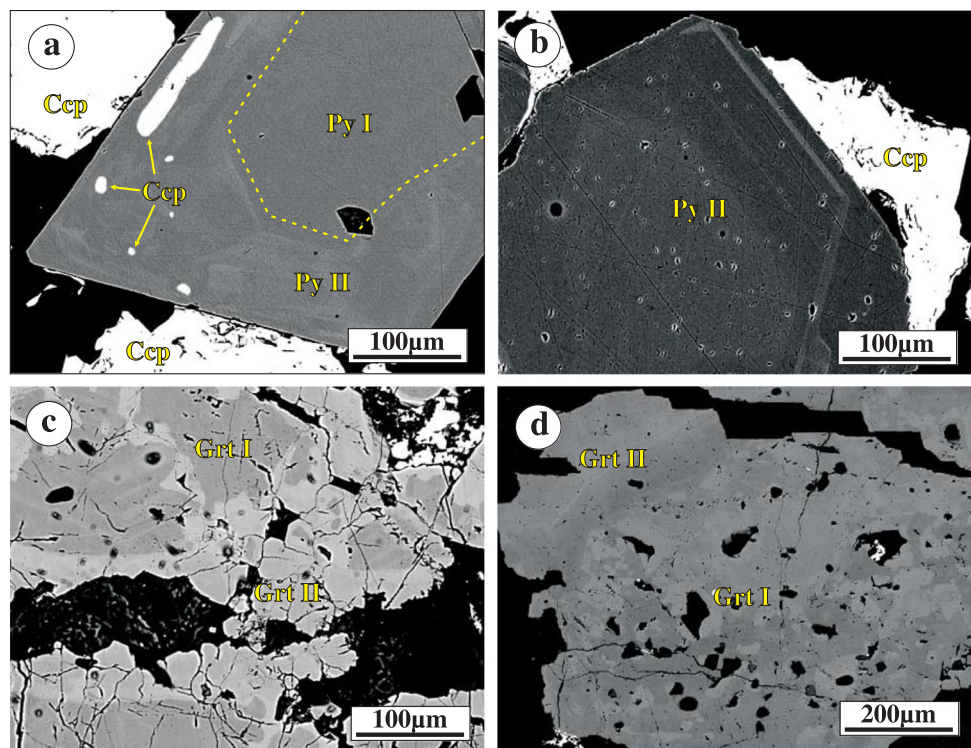
of $^{187}Re/^{188}Os$ versus $^{187}Os/^{188}Os$ of these samples, yielding a 5-point regression of 892 ± 200 Ma (MSWD = 21), if the outlier sample SL11-33 is excluded (Fig. 8a).

Six pyrite separates of stage III Cu-Co ores have similarly low ^{187}Re (0.11 to 11.5 ppb) and ^{187}Os (0.01 to 0.19 ppb) (ESM Table 3). They have also a range of $^{187}Re/^{188}Os$ ratios (30.6–879) that are much lower than 5000 (Stein et al. 2001), and variable model ages of 659 to 851 Ma (ESM Table 3). The $^{187}Re/^{188}Os$ versus $^{187}Os/^{188}Os$ plot yields an isochron age of 780 ± 24 Ma with a MSWD value of 0.62 (Fig. 8b).

Garnet U–Pb isotopic ages

Two samples, SL11-4–1 and SL11-38–1, were selected for in situ garnet U–Pb dating (ESM Table 4). Both samples are garnet-bearing Fe ores that are foliated and contain extensively elongated garnet patches (e.g., Fig. 2g). The garnet has likely undergone extensively recrystallization, as the crystals generally contain BSE-inhomogeneous cores with abundant inclusions of minerals that are associated with Fe-Cu-Co mineralization, surrounded by BSE-homogeneous/oscillatory overgrown rims (e.g., Fig. 7c and d). Both the core and rims were analyzed in this study, but only the rims exhibit stable elemental signals during laser ablation. Garnet rims in both samples have comparable U contents ranging from 0.7 to 1.21 and 0.57 to 1.99 ppm, respectively. A total of 20 analyses are obtained for the rims in the sample

SL11-4–1, and most of them yield discordant U–Pb ages (Fig. 8c). However, in the Tera-Wasserburg diagram, these analyses form a good linear array that gives a lower-intercept age of 266 ± 20 Ma (1σ, MSWD = 0.35) if the two relatively scattered data points 06 and 13 (Fig. 8c) are excluded. On the other hand, a total of 15 analyses are obtained for the rims in the sample SL11-38–1, and most of them are discordant. Similar to the sample SL11-4–1, these analyses form a good array in the Tera-Wasserburg diagram, and yield a lower-intercept age of 247 ± 14 Ma (1σ, MSWD = 0.43) if data point 04 is excluded (Fig. 8d).
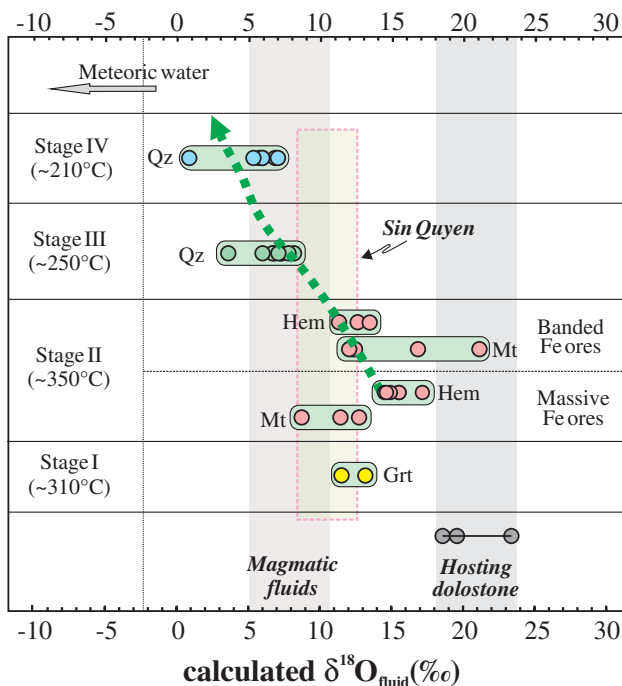
Isotope geochemistry

Detailed analytical methods for oxygen isotope analysis of different minerals and in situ Pb–S isotopes of sulfides are available in Appendix I, and the obtained O, Pb, and S isotopic compositions are provided in Electronic Supplementary Materials (i.e., ESM Tables 5, 6, and 7, respectively). Note that the O isotopic data of Xu et al. (2013) and Yu et al. (2014) are also combined by re-correlating them with the paragenetic sequence established in this study (Fig. 9). The isotope fractionation factors used for the calculation of fluid $\delta^{18}O$ values are provided in ESM Table 5, and the temperatures used for the calculation refer to the fluid inclusion data (i.e., homogenization temperatures) of different minerals by Yu et al. (2014).

Fig. 8 Sulfide Re-Os and in situ garnet U–Pb isotopic analyses of the Shilu deposit. **a**) Re-Os regression of early sedimentary pyrite; **b**) Re-Os isochron age of stage III pyrite; **c**) and **d**) Tera–Wasserburg diagram for garnet grains from samples SL11-38–1 and SL11-4–1
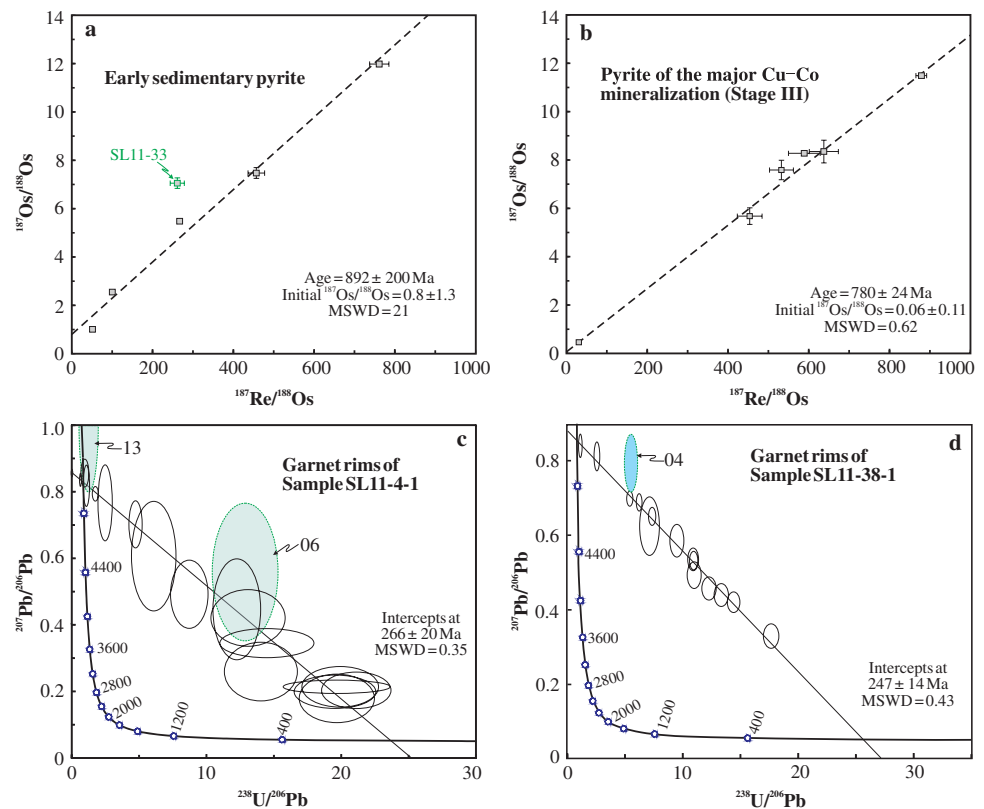
Oxygen isotopic composition of minerals

Two garnet separates of stage I have comparable $\delta^{18}O$ values of 10.9 and 9.2‰. Using the estimated temperature of ~310 °C (estimated by fluid inclusions in garnet of skarn-stage documented in Yu et al. 2014), the $\delta^{18}O$ values of stage I fluids were calculated to be 11.4 to 13.1‰. Hematite and magnetite of the massive Fe ores have $\delta^{18}O$ values ranging from 4.7 to 7.3 ‰ and 0.3 to 4.3 ‰, respectively (ESM Table 5). Using the temperature of ~350 °C estimated by fluid inclusions in epidote (Yu et al. 2014), the $\delta^{18}O$ values of the fluids were calculated to vary from 14.7 to 17.2 ‰ for hematite and 8.5 to 12.5 ‰ for magnetite. On the other hand, magnetite and hematite from banded Fe ores have comparable $\delta^{18}O$ values ranging from 3.6 to 12.7 ‰ and 3.1 to 5.2 ‰, respectively, corresponding to calculated $\delta^{18}O$ values of the fluids ranging from 11.8 to 20.9 ‰ and 11.3 to 13.4 ‰, respectively, using the same temperature of ~350 °C (ESM Table 5; Fig. 9).

The $\delta^{18}O$ values of quartz in stage III Cu-Co mineralization vary from 12.5 to 17.1 ‰, corresponding to calculated $\delta^{18}O$ values of fluids (using 250 °C that is estimated by fluid inclusions in the skarn-stage quartz documented in Yu et al. 2014) ranging from 3.5 to 8.1 ‰ (ESM Table 5). On the other hand, quartz from stage IV veins has $\delta^{18}O$ values varying from 11.9 to 18.1 ‰, and the calculated $\delta^{18}O$ values of fluids (using 210 °C estimated by fluid inclusions in quartz

Fig. 9 Diagram showing calculated $\delta^{18}O$ values of fluids based on minerals in the Shilu deposit. Also shown are the $\delta^{18}O$ values of magmatic fluids, host dolostone/marble (Xu et al. 2013), and mineralizing fluids of the Sin Quyen deposit (Li and Zhou 2018)

of late veins in Yu et al. 2014) range from 0.8 to 7.0 ‰, slightly lower than those of stage III fluids (ESM Table 5; Fig. 9).

In situPb–S isotopic composition of sulfides

Pyrite grains of the earliest massive bands or patches have $^{206}Pb/^{204}Pb$, $^{207}Pb/^{204}Pb$, and $^{208}Pb/^{204}Pb$ ratios varying from 18.104 to 19.232, 15.456 to 15.896, and 36.531 to 37.885, respectively (ESM Table 6; Fig. 10a and b), and $\delta^{34}S$ values ranging from + 13.1 to + 19.0 (ESM Table 7; Fig. 11). In contrast, stage III sulfides have remarkably lower $^{206}Pb/^{204}Pb$ (17.312–18.240), $^{207}Pb/^{204}Pb$ (15.283–15.688), and $^{208}Pb/^{204}Pb$ (35.888–37.173) ratios (Fig. 10; ESM Table 6), and relatively low but highly variable $\delta^{34}S$ values (+ 1.9 to + 15.7) (ESM Table 7; Fig. 11). On the other hand, sulfides from stage IV veins have a relatively large range of
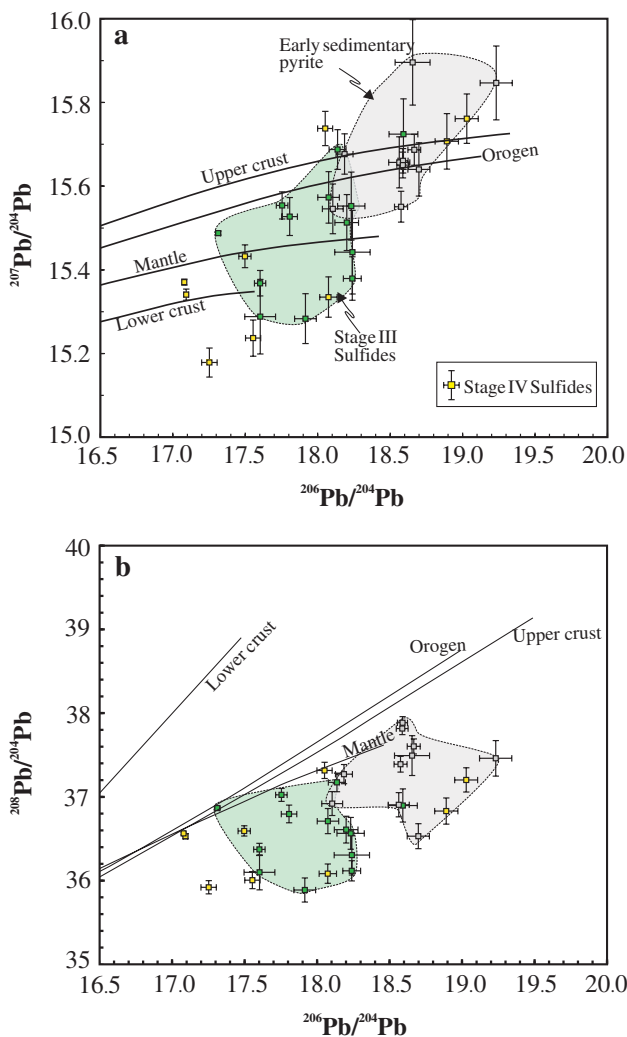
Fig. 10 Plots of $^{207}Pb/^{204}Pb$ (**a**) and $^{208}Pb/^{204}Pb$ (**b**) versus $^{206}Pb/^{204}Pb$ of different generations of sulfides in the Shilu deposit
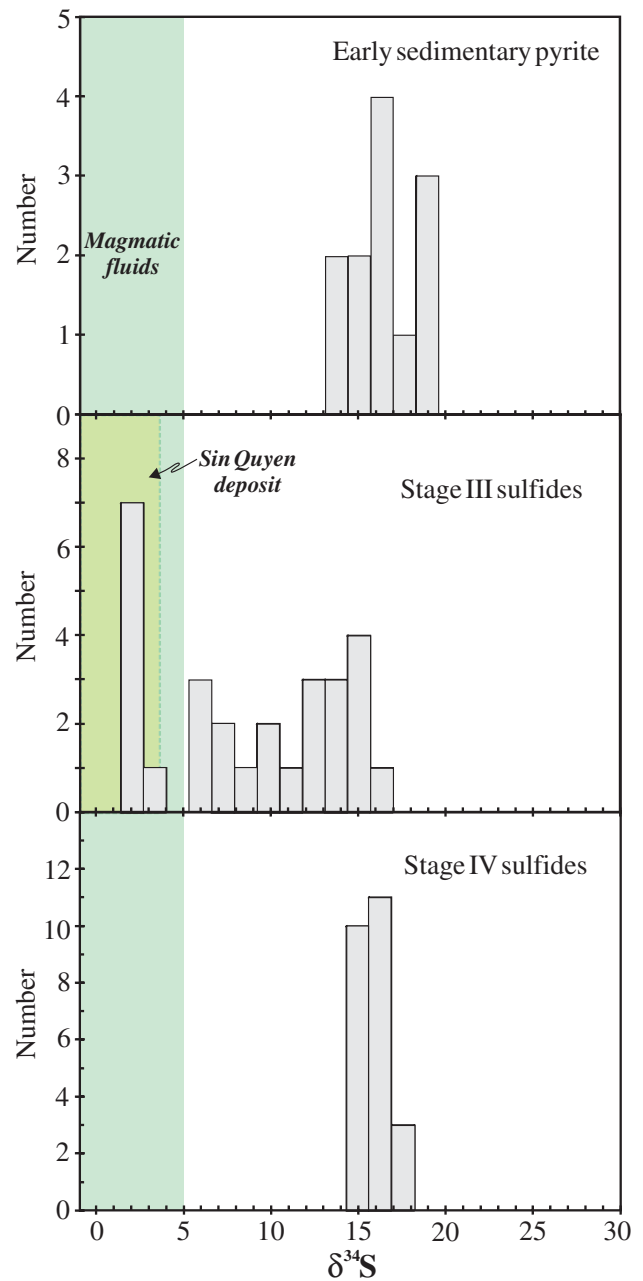
Fig. 11 Histograms showing $\delta^{34}S$ values of different generations of sulfides in the Shilu deposit. Also shown are the $\delta^{34}S$ values of magmatic fluids and sulfides of the Sin Quyen deposit (Li and Zhou 2018)

$^{206}Pb/^{204}Pb$ (17.312–18.240), $^{207}Pb/^{204}Pb$ (15.283–15.688), and $^{208}Pb/^{204}Pb$ (35.888–37.173) ratios which almost cover those of sulfides from the early stages (Fig. 10; ESM Table 6). However, they have a limited range of $\delta^{34}S$ values (+ 15.0 to + 17.1) (ESM Table 7), higher than stage III sulfides but broadly similar to the early sedimentary pyrite (Fig. 11).

Discussion

Nature of multi-stage mineralization in the Shilu deposit

Although the ores/host rocks were variably deformed or hydrothermally overprinted, this study did identify a number of primary macro- and micro-textures that convincingly suggest that the major Fe-Cu-Co mineralization postdates the deposition of the host rocks and is supposed to be hydrothermal in origin (e.g., Figs. 2a–h and 3a–c). For example, the identified rounded quartz grains and/or patches in massive Fe ores, which are likely relics of sandstones, are disturbed or cemented by a matrix of hematite/magnetite (e.g., Fig. 3a, b, and c). Our results do show that the massive Fe ores have Fe oxides trace elemental compositions undistinguishable from those of the banded Fe ores associated with skarns (e.g., garnet, diopside, chlorite, and epidote) (Figs. 5 and 6). Moreover, the widespread garnet and diopside which were previously considered to be of metamorphic origin in the BIF model were confirmed to texturally predate the deformation and have chemical compositions particularly similar to those of typical Fe skarn deposits worldwide (ESM Table 1), and thus can be redefined as hydrothermal in origin. These new findings together strongly support that both the banded and massive Fe ores do not belong to BIFs as previously proposed (e.g., Xu et al., 2015) but are epigenetic and formed from a co-genetic hydrothermal fluid. Indeed, unlike stratiform ones such as BIFs that extend along with the host strata in a regional scale, Fe ores in Shilu are only confined within a strongly altered zone. It is important to mention that the trace element signature of the Fe oxides should be original with limited modification during post-ore metamorphism or hydrothermal overprints. The reason is that both the magnetite and hematite in the banded Fe ores with more complicated mineral assemblages do not exhibit expected large elemental differences (e.g., elemental diffusion) when compared to those in the massive Fe ores with gangue minerals as mainly "trace element-barren" quartz (Figs. 5 and 6).

The fluids of stages I and II have comparable $\delta^{18}O$ values (ESM Table 5; Fig. 9) that fall in the fields between typical magmatic fluids (5–10‰) and host dolostones (18.5–23.3 ‰; Xu et al. 2013). This feature indicates contributions of oxygen from both magmatic fluids and host rocks through extensive fluid-rocks interaction that is responsible for the formation of the "diopside-amphibole-rich host rocks" (i.e., stage I Ca-silicate alteration) and accompanied Fe mineralization (i.e., stage II). It is notable that the magnetite grains in the banded and massive Fe ores in stage II have Ti and Al contents consistently lower than the hematite but exhibiting a clear positive correlation (Fig. 5a, b). On the basis of the

fact that the magnetite in both types of ores slightly post-dates the hematite (Fig. 3d), we propose that such chemical variations of Fe oxides are mainly due to different stages in fluid evolution, i.e., hematite precipitated before magnetite (Nadoll et al. 2014).

Stage III fluids have calculated $\delta^{18}O$ values (3.5 to 8.1 ‰) broadly similar to typical magmatic fluids (Fig. 9), indicative of a dominant magmatic source. The relatively low value (3.5‰) of sample SL10-27 possibly indicates additional contribution of meteoric water (Fig. 9). On the other hand, in situ sulfide S isotopic ratios show large ranges covering those of the magmatic fluids and earliest pyrite in massive bands (Figs. 10 and 11), indicating contributions of sulfur from both potential sources.

Stage IV fluids for the late undeformed veins have calculated $\delta^{18}O$ values (0.8 to 7.0 ‰) suggestive of contributions of magmatic and meteoric water (Fig. 9). The Pb–S isotopic ratios cover those of stages III and early massive pyrite (Figs. 10 and 11), indicating contributions of Pb and S from early-stage components. These geochemical features, in combination with the fact that these undeformed, root-less veins have diverse mineral assemblages almost covering those of early pre-deformation stages (e.g., Fig. 2f and l) (Xu et al. 2009, 2013; Yu et al. 2014; Wang et al. 2015a), thus support their formation from early components through remobilization triggered by late metamorphism or hydrothermal overprints.

Timing of multiple mineralization/overprint events

By incorporating data of Zhang et al. (1992), Xu et al. (2013) have reported a Sm–Nd isochron age of 830 ± 16 Ma for Fe ores and diopside-amphibole-rich dolostones, but they did not provide the exact paragenetic relationships of these samples. Instead, another similar Sm–Nd isotopic study did not obtain an expected similar age but yet gave a much younger isochron age of 212.9 ± 6.6 Ma (Xu et al. 2013). Such an age is broadly similar to Ar–Ar ages of 210 to ~130 Ma (Xu et al. 2007, 2013), and were thus suggested to be resetting ages likely related to emplacement of the nearby granitoids (240–90 Ma). In addition, both Xu et al. (2015) and Wang et al. (2015c) reported EMPA chemical U–Pb ages of monazite grains in host rocks and ores. These ages are highly variable from 1270 to 240 Ma with peaks at 460 and 260 Ma, of which the latter peak is consistent with our in situ garnet U–Pb ages (250–260 Ma) (Fig. 8c and d). Considering that the dated minerals (e.g., monazite and garnet) are variably recrystallized (e.g., Figs. 2g–h and 7), it is proposed that the two age peaks should represent the timing of late overprints possibly related to Caledonian and Indosinian orogenic events documented in the region (Wang et al. 2015c; Xu et al. 2015).

In this study, we obtained Re-Os ages of pyrite from the early massive pyrite bands and stage III Cu-Co ores, as it was commonly accepted that the Re-Os isotopic system of sulfides was generally stable even under high-grade metamorphism (Stein et al., 2001) and thus is able to record the timing of pre-deformation Fe-Cu-Co mineralization. The analyses for the early pyrite in massive bands, which are sedimentary in origin (Wang et al., 2015a), yield a Re-Os errorchron age of 892 ± 200 Ma without clear geological meanings (Fig. 6a). This situation is possibly ascribed to the low Os contents of the pyrite and the inherent low precision of the analysis by quadrupole ICP-MS, or extensive modification on pyrite (Wang et al. 2015a). In contrast, the six pyrite separates of stage III Cu-Co ores have a good Re-Os isochron age of 780 ± 24 Ma (Fig. 8b) that is broadly comparable to the Sm–Nd isochron age obtained by Xu et al. (2013), thus being considered to be the timing of the pre-deformation Fe-Cu-Co mineralization. It is important to note that potential risks of suffering from variable degrees of hydrothermal overprints (e.g., forming core-rim-textural pyrite; Fig. 7a) (Wang et al. 2015a) were avoided in this study by only selecting the samples that exhibit slight deformation and do not contain any late veinlets, to ensure that the selected pyrite grains are broadly homogeneous under BSE images (Fig. 7b).

In summary, this study provides a good example that the primary Re-Os isochron age could be well retained during secondary modification (i.e., without significant gain or loss of Re and Os in whole rock/ore scales), whereas the U–Pb systems of garnet and monazite that are variably recrystallized (e.g., Figs. 2g–h and 7c, d) were variably reset, thus recording multiple regional overprint events (Wang et al. 2015c; Xu et al. 2015). Such a situation is common in other superimposed deposits, such as the giant Bayan Obo Fe-REE-Nb deposit of which the Sm–Nd isochron ages record the timing of primary mineralization while the U-Th-Pb ages of monazite are fully or partially reset due to variable degrees of recrystallization (Li et al. 2021).

### A genetic model for the Shilu Fe-Cu-Co deposit

On the basis of the new results mentioned above, we propose a new genetic model which is comparable to those of magmatic-hydrothermal deposits (ESM Figures) (Xu et al. 2008a, b; Du et al. 2012). Early geochronological studies well constrained that the Shilu Group was deposited at around 900 Ma (Xu et al. 2013; Wang et al. 2015b; Zou et al. 2017). Subsequent invasion of ~780 Ma magma-derived, mineralizing fluids along fracture zones or lithological contacts in the Shilu Group (e.g., the ore bodies are mostly strata-bound; Fig. 1d) has produced early Fe oxide and late Cu-Co sulfide mineralization, associated with extensive fluid-rocks interaction forming the Ca-silicate alteration

(ESM Figures). Late overprint events of Caledonian and Indosinian ages (e.g., 590–450 or 260–210 Ma) have variably modified the early Fe-Cu-Co ores (ESM Figures), and the latter event was likely responsible for the formation of the diverse, undeformed veins of stage IV (Fig. 2f and l) (Yu et al. 2014).

We further propose that the pre-deformation Fe-Cu-Co mineralization in the Shilu deposit shares many features with typical magmatic-hydrothermal IOCG deposits. For example, there are abundant relatively Ti-poor hematite and magnetite ($TiO_2 < 1$wt.%), together with Cu mineralization and variable enrichments of Co, Ni, Ag, Au, and As (Xu et al. 2008a; Wang et al. 2015b), comparable to IOCG deposits but dramatically different from BIFs. The paragenetic sequence, which includes an early oxide stage forming massive Fe ores and a late sulfide stage introducing Cu-Co mineralization (Fig. 4), and the fluid evolution process, which involves significant contributions of magmatic and external components (e.g., host rocks, sedimentary sulfur, meteoric water) (Figs. 9, 10, and 11), are also comparable to those of IOCG deposits worldwide (e.g., Hitzman et al. 1992; Groves et al. 2010). Although the Ca-silicate alteration in the Shilu deposit has produced skarns (e.g., garnet and diopside), these can be produced by interaction of fluids with carbonate rocks. For example, skarns were also reported in the Candelaria IOCG deposit in Chile (Ray and Lefebure 2000) and the Sin Quyen deposit in the LSQ IOCG belt (Li et al. 2018a; Li and Zhou 2018). Indeed, it is clearly shown that the Shilu deposit does not show any evidence for the close spatial association of alteration with plutons and there is no alteration zonation common in skarn deposits. Moreover, the Fe oxides in the Shilu deposit have trace elemental compositions more alike typical IOCG deposits, but remarkably different from typical BIFs or skarn deposits (Fig. 12).

Implications for the potential linkage of the Shilu deposit with the Longbohe-Sin Quyen (LSQ) IOCG belt

Our new results confirm that the major mineralization in the Shilu deposit was related to a Neoproterozoic IOCG-style hydrothermal system (ESM Figures), and not to a BIF system as previously proposed. The IOCG system was then overprinted by early Paleozoic to late Mesozoic tectonothermal events. However, similar Fe-Cu-Co deposits of Proterozoic age are not known on Hainan Island so far, nor other exposures of the ~0.9 Ga Shilu Group or potential causative ~780 Ma igneous plutons (e.g., Zhang et al. 2011; Xu et al. 2013). Therefore, it is unclear if the Fe-Cu-Co mineralization event was regional. At Proterozoic, Hainan Island was traditionally considered to be correlated with the Cathaysia Block of the South China Craton (e.g., Li et al. 2002, 2008), but this view was refuted by recent
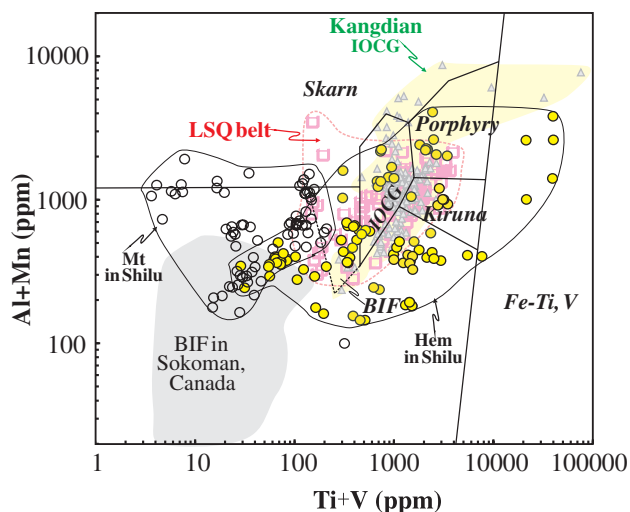
Fig. 12 Plot of V + Ti vs. Al + Mn of magnetite/hematite from different types of Fe ores in the Shilu deposit. Note that the hematite/magnetite data from Shilu exclude a BIF origin because they cover the full temperature spread defined by porphyry deposits to BIF, recording a consecutive evolution of magmatic fluids. The data are also not consistent with a skarn in origin due to the relatively low Al + Mn contents. Reference fields are after Dupuis and Beaudoin (2011). BIF, banded iron formation; Skarn, Fe-Cu skarn deposits; IOCG, iron-oxide-copper–gold deposits; Porphyry, porphyry Cu deposits; Kiruna, Kiruna apatite-magnetite deposits; Fe-Ti, V, Fe-Ti-oxide deposits. The trace elemental data of IOCG deposits in the Kangdian and Longbohe-Sin Quyen belts are from Chen et al. (2015) and our unpublished data, respectively, and those of BIF in Sokoman are from Chung et al. (2015)

studies on detrital zircon ages that strongly indicate that southern Hainan is more likely connected with the southwestern Yangtze Block of the South China Craton within the Rodinia (EMS Figures) (Zhang et al. 2020), or western Laurentia within the Columbia supercontinents (Wang et al. 2015b; Xu et al. 2020). Indeed, increasing evidence did confirm that the Cenozoic, > 1000-km-long ASRR shear zone extends to the Shilu region of Hainan Island before being rifted away during Tertiary spreading of the South China Sea (Fig. 1b) (Replumaz and Tappinnier 2003; Chen et al. 2013; Zhou et al. 2014; Liu and Chen 2019; Zhang et al. 2020). In particular, the ASRR shear zone on the mainland side (northern Vietnam and southern Yunnan, China) contains numerous Neoproterozoic strata (~ 900 Ma) and intrusions (740–860 Ma), as well as a number of Proterozoic IOCG-type Fe-Cu deposits or prospects defining the economically important Longbohe-Sin Quyen (LSQ) metallogenic belt (ESM Figures) (Li et al. 2018a; Liu and Chen 2019). These features allow us to propose that the Shilu deposit is probably part of the LSQ metallogenic belt (ESM Figures). Such a proposal is well supported by the similarities of ore-hosting rocks, mineralization, Fe-oxide compositions, and late

Paleozoic geology (e.g., Figs. 9, 11, and 12), which are also illustrated in detail in Electronic Supplementary Materials (i.e., Appendix II and ESM Figures).

Concluding remarks

Our study provides convincing evidence for the epigenetic origin of the Fe-Cu-Co mineralization in the giant Shilu deposit that formed at ~ 780 Ma in a partly exposed IOCG system, followed by early Paleozoic and late Mesozoic tectonothermal-hydrothermal overprints. The primary mineralization has a paragenetic sequence including an earliest, Ca-silicate alteration stage with abundant garnet, diopside, and amphibole, followed by early Fe oxide and late Cu-Co sulfide mineralization stages. The hydrothermal fluids for the Fe and Cu-Co mineralization were initially high-temperature, magmatic fluids that subsequently interacted extensively with the host rocks of the Shilu Group (e.g., dolostones/marble and/or sandstone). These new results, as well as elevated Ti contents in hematite, argue against the previously hold model of BIF-type mineralization. It also cannot be a skarn-type deposit, as the ore bodies do not have clear spatial association with causative intrusion and typical alteration zonation similar to a skarn deposit is not developed. Instead, the Shilu deposit shares many characteristics with IOCG deposits elsewhere. In particular, the deposit is comparable to the Neoproterozoic IOCG deposits of the LSQ belt in the ASRR shear zone, in terms of host rock lithology, timing and nature of mineralization, and late Paleozoic geology. These similarities suggest that the IOCG mineralization in both regions is likely correlated. Given that the ASRR shear zone was confirmed to extend to Hainan Island, such a correlation implies that similar mineralization in the shear zone is likely more widespread than previously thought, particularly in the sections between the Shilu and Sin Quyen regions where levels of exploration are currently low.

Declarations

Conflict of interest The authors declare no competing interests.

References

Cai YF, Wang YJ, Cawood PA, Zhang YZ, Zhang AM (2015) Neoproterozoic crustal growth of the Southern Yangtze Block: geochemical and zircon U-Pb geochronological and Lu-Hf isotopic evidence of Neoproterozoic diorite from the Ailaoshan zone. Precambr Res 266:137–149

Chen WT, Zhou MF, Gao JF, Hu RZ (2015) Geochemistry of magnetite from Proterozoic Fe-Cu deposits in the Kangdian metallogenic province, SW China. Miner Deposita 50:795–809

Chen ZC, Lin W, Faure M, Lepvrier C, Chu Y, Wang QC (2013) Geochronological constaint of early Mesozoic tectonic event at Northeast Vietnam. Acta Petrologica Sinica 29:1825–1840

Chung SL, Lee TY, Lo CH, Wang PL, Cheng CY, Nguyen TH, Tran TH, Wu GY (1997) Intraplate extension prior to continental extrusion along the Ailao Shan-Red River shear zone. Geology 25:311–314

Chung D, Zhou MF, Gao JF, Chen WT (2015) In-situ LA-ICP-MS trace elemental analyses of magnetite: the late Palaeoproterozoic Sokoman Iron Formation in the Labrador Trough, Canada. Ore Geol Rev 65:917–928

Dare SAS, Barnes SJ, Beaudoin G, Meric J, Boutroy E, Potvin-Doucet C (2014) Trace elements in magnetite as petrogenetic indicators. Miner Deposita 49:785–796

Du BF, Wei JH, Shi WJ, Zhao SQ, Wang YH, Yi J (2012) Comparisons between the Shilu Fe-Co-Cu-(Au) deposit in Hainan Province and other IOCG-type deposits at home and abroad. Geol Exploration 48:332–343 (in Chinese with English abstract)

Dupuis C, Beaudoin G (2011) Discriminant diagrams for iron oxide trace element fingerprinting of mineral deposit types. Miner Deposita 46:319–335

Guangdong BGMR (Bureau of Geology Mineral Resources) (1988) Regional Geology of Guangdong Province. Geological Publishing House, Beijing, pp 602 (in Chinese)

Groves DI, Bierlein FP, Meinert LD, Hitzman MW (2010) Iron oxide copper-gold (IOCG) deposits through earth history: implications for origin, lithospheric setting, and distinction from other epigenetic iron oxide deposits. Econ Geol 105:641–654

He H, Wang Y, Qian X, Zhang Y (2018) The Bangxi-Chenxing tectonic zone in Hainan Island (South China) as the eastern extension of the Song Ma-Ailaoshan zone: evidence of late Paleozoic and Triassic igneous rocks. J Asian Earth Sci 164:274–291

Hieu PT, Chen FK, Zhu XY, Wang F, Nguyen TBH, Bui MT, Nguyen QL (2009) Zircon U-Pb ages and Hf isotopic composition of the Posen granite in northwestern Vietnam. Acta Petrol Sin 25:3141–3152 (in Chinese with English Abstract

Hitzman MW, Oreskes N, Einaudi MT (1992) Geological characteristics and tectonic setting of Proterozoic iron oxide (Cu-U-Au-REE) deposits. Precambr Res 58:241–287

Hsü KJ, Li JL, Chen HH, Wang QC, Sun S, Sengor AMY (1990) Tectonics of South China: key to understanding west Pacific geology'. Tectonophysics 193:9–39

Li XC, Zhou MF, Chen WT, Zhao XF, Tran M (2018) Uranium-lead dating of hydrothermal zircon and monazite from the Sin Quyen Fe-Cu-REE-Au-(U) deposit, northwestern Vietnam. Miner Deposita 533:399–416

Li XC, Zhao JH, Zhou MF, Gao JF, Sun WH, Tran MD (2018) Neoproterozoic granitoids from the Phan Si Pan belt, Northwest Vietnam: implication for the tectonic linkage between Northwest Vietnam and the Yangtze Block. Precambr Res 309:212–230

Li XC, Zhou MF (2018) The nature and origin of hydrothermal REE mineralization in the Sin Quyen deposit, northwestern Vietnam. Econ Geol 113:645–673

Li XC, Yang KF, Spandler C, Fan HR, Zhou MF, Hao JL, Yang YH (2021) The effect of fluid-aided modification on the Sm-Nd and Th-Pb geochronology of monazite and bastnäsite: implication for resolving complex isotopic age data in REE ore systems. Geochim Cosmochim Acta 300:1–24

Li XH, Zhou HW, Chung SL, Ding SJ, Liu Y, Lee CY, Ge WC, Zhang YM, Zhang RJ (2002) Geochemical and Sm-Nd isotopic characteristics of metabasites from central Hainan Island, South China and their tectonic significance. Island Arc 11:193–205

Li XH, Zhou HW, Ding SJ, Li J, Zhang RJ, Zhang YM, Ge WC (2000) Metamorphosed mafic rocks with N-type MORB geochemical features in Hainan Island: remnants of the Paleo-Tethys oceanic crust? Chin Sci Bull 45:84–88 (in Chinese)

Li ZX, Li XH, Li WX, Ding SJ (2008) Was Cathaysia part of Proterozoic Laurentia? – new data from Hainan Island, South China. Terra Nova 20:154–164

Liu L, Chen WT (2019) Geology, mineralization styles and age of ore-hosting rocks of the Proterozoic Longbohe-Sin Quyen Fe-Cu belt: implications for regional metallogeny. Ore Geol Rev 111:103013

Nadoll P, Angerer T, Mauk JL, French D, Walshe J (2014) The chemistry of hydrothermal magnetite: a review. Ore Geol Rev 61:1–32

Ray GE, Lefebure DV 2000 A synopsis of iron oxide Cu Au P REE deposits of the Candelaria-Kiruna-Olympic Dam family. British Columbia Ministry of Energy and Mines, pp. 267–272.

Replumaz A, Tapponnier P (2003) Reconstruction of the deformed collision zone between India and Asia by backward motion of lithospheric blocks. J Geophys Res 108:1–24

Searle MP, Yeh MW, Lin TH, Chung SL (2010) Structural constraints on the timing of left-lateral shear along the Red River shear zone in the Ailao Shan and Diancang Shan Ranges, Yunnan, SW China. Geosphere 6:316–338

Slack JF (2012) Stata-bound Fe-Co-Cu-Au-Bi-Y-REE deposits of the Idaho cobalt belt: multistage hydrothermal mineralization in a magmatic-related iron oxide copper-gold system. Econ Geol 107:1089–1113

Stein HJ, Markey RJ, Morgan JW, Hannah JL, Schersten A (2001) The remarkable Re-Os chronometer in molybdenite: how and why it works. Terra Nova 13:479–486

Wang XF, Ma DQ, Jiang DH (1991) Geology of Hainan Island: structural geology. Geological Publish House, Beijing (in Chinese)

Wang YJ, Zhou YZ, Cai YF, Liu HC, Zhang YZ, Fan WM (2016) Geochronological and geochemical constraints on the petrogenesis of the Ailaoshan granitic and migmatite rocks and its implications on Neoproterozoic subduction along the SW Yangtze Block. Precambr Res 283:106–124

Wang ZL, Xu DR, Hu GC, Yu LL, Wu CJ, Zhang ZC, Cai JX, Shan Q, Hou MZ, Chen HY (2015) Detrital zircon U-Pb ages of the Proterozoic metaclastic-sedimentary rocks in Hainan Province of South China: new constraints on the depositional time, source area, and tectonic setting of the Shilu Fe–Co–Cu ore district. J Asian Earth Sci 113:1143–1161

Wang ZL, Xu DR, Zhang YQ, Chen FX, Wang L, Wu J (2011) Zircon LA-ICP-MS U-Pb dating of the granodiorite porphyry from Shilu iron ore deposit, Hainan Province and its geological implication. Geotecton Metallog 35:292–299 (in Chinese with English abstract)

Wang ZL, Xu DR, Zhang ZC, Zou FH, Wang L, Yu LL, Hu MY (2015) Mineralogy and trace element geochemistry of the Co- and Cu-bearing sulfides from the Shilu Fe-Co-Cu ore district in Hainan Province of South China. J Asian Earth Sci 113:980–997

Wang ZL, Xu DR, Monika AK, Wu CJ, Yu LL (2015) Genesis of and CHIME dating on monazite in the Shilu iron ore deposit, Hainan Province of South China, and its geological implications. Acta Petrologica Sinica 31(1):200–216

Xiao Y, Cai RJ, Fu QJ, Liu ZL, Wu ZC, Chen BJ (2010) Geological characteristics and prospecting orientation of Shilu iron, cobalt and copper polymetallic ore accumulation zone. Mineral Resources and Geology 24:251–255 (in Chinese with English abstract)

Xu DR, Kusiak MA, Wang ZL, Chen HY, Bakun-Czubarow N, Wu CJ, Konecny P, Hollings P (2015) Microstructural observation and chemical dating on monazite from the Shilu Group, Hainan Province of South China: implications for origin and evolution of the Shilu Fe-Co-Cu ore district. Lithos 216–217:158–177

Xu DR, Wang L, Xiao Y, Liu CL, Fu QJ, Cai ZR, Huang JR (2008) A preliminary discussion on metallogenic model for Shilu-type iron oxide copper-gold-cobalt ore deposit. Mineral Deposits 27:681–694 (in Chinese with English abstract)

Xu DR, Wang ZL, Cai JX, Wu CJ, Bakun-Czubarow N, Wang L, Chen HY, Baker MJ, Kusiak MA (2013) Geological characteristics and metallogenesis of the Shilu Fe-ore deposit in Hainan Province, South China. Ore Geol Rev 53:318–342

Xu DR, Wang ZL, Chen HY, Hollings P, Jansen NH, Zhang ZC, Wu CJ (2014) Petrography and geochemistry of the Shilu Fe-Co-Cu ore district, South China: implications for the origin of a Neoproterozoic BIF system. Ore Geol Rev 57:322–350

Xu DR, Xia B, Li PC, Chen GH, Ma C, Zhang YQ (2007) Protolith natures and U-Pb sensitive high mass-resolution ion microprobe (SHRIMP) zircon ages of the metabasites in Hainan Island, South China: implications for geodynamic evolution since the late Precambrian. Island Arc 16:575–597

Xu DR, Xia B, Nonna BC, Bachlinski R, Li P, Chen G, Chen T (2008) Geochemistry and Sr-Nd isotope systematics of metabasites in the Tunchang area, Hainan Island, South China: implications for petrogenesis and tectonic setting. Mineral Petrol 92:361–391

Xu DR, Xiao Y, Xiao B, Cai RJ, Hou W, Wang L, Liu ZL 2009 Metallogenic model and ore predicating of the Shilu iron ore deposit in Hainan Province, China. Geol Publishing House, Beijing, pp. 1–331 (in Chinese).

Xu Y, Cawood PA, Zhang H, Zi J, Zhou J, Li L, Du Y (2020) The Mesoproterozoic Baoban Complex, South China: a missing fragment of western Laurentian lithosphere. Geol Soc Am Bull 132:404–1418

Yu JJ, Chen FX, Wang YH, Liang J, Che LR (2012) Origin and rock-forming environment of Indosinian granite in the Shilu iron ore district and its peripheral region. Geol China 39:1700–1711 (in Chinese with English abstract)

Yu JJ, Mao JW, Chen FX, Wang YH, Che LR, Wang TZ, Liang J (2014) Metallogeny of the Shilu Fe-Co-Cu deposit, Hainan Island, South China: constraints from fluid inclusions and stable isotopes. Ore Geol Rev 57:351–362

Zhang F, Wang Y, Chen X, Fan W, Zhang Y, Zhang G, Zhang A (2011) Triassic high-strain shear zones in Hainan Island (South China) and their implications on the amalgamation of the Indochina and South China Blocks: kinematic and $^{40}Ar/^{39}Ar$ geochronological constraints. Gondwana Res 19:910–925

Zhang RJ, Ma GC, Hong SN, Yan DP (1992) The Sm-Nd isotopic age of Shilu iron ore in Hainan Island and its implications. Sci Geol Sin 21:38–43 (in Chinese with English abstract)

Zhang L, Cawood PA, Wang Y, Cui X, Zhang Y, Qian X, Zhang F 2020 Provenance record of late Mesoproterozoic to early Neoproterozoic units, west Hainan, South China, and implications for Rodinia reconstruction. Tectonics 39, in press.

Zhao JH, Zhou MF, Yan DP, Zheng JP, Li JW (2011) Reappraisal of the ages of Neoproterozoic strata in South China: no connection with the Grenvillian orogeny. Geology 39:299–302

Zhao JS, Xia B, Qiu XL, Zhao B, Xu DR, Feng ZH, Li ZL, Shen GF, Hu RZ, Su WC, Qin CJ, Qin WM, Fu X, Hu ZG (2008) Finding of melt inclusion in garnet from skarn of Shilu iron deposit, Hainan province. Acta Petrologica Sinica 24:149–160 (in Chinese with English abstract)

Zhou MF, Zhao XF, Chen WT, Li XC, Wang W, Yan DP, Qiu HN (2014) Proterozoic Fe-Cu metallogeny and supercontinental cycles of the southwestern Yangtze Block, southern China and northern Vietnam. Earth Sci Rev 139:59–82

Zou SH, Yu LL, Yu DS, Xu DR, Ye TW, Wang ZL, Cai JX, Liu M (2017) Precambrian continental crust evolution of Hainan Island in South China: constraints from detrital zircon Hf isotopes of metaclastic-sedimentary rocks in the Shilu Fe-Co-Cu ore district. Precambr Res 296:195–207